PAST KNOWLEDGE PEOPLE

ISSN: 2993-5326

Research Article

Journal of Applied Surface Science

Simulation of the Moiré Effect in a Volumetric Cube. Part II: Edge and Vertex Views

Vladimir Saveljev*

Independent researcher, Daejeon, Republic of Korea

***Corresponding Author**
Vladimir Saveljev, Independent researcher, Daejeon, Republic of Korea.

Submitted: 2026, Sep 16; **Accepted:** 2026, Oct 22; **Published:** 2026, Nov 06

Citation: Saveljev, V. (2026). Simulation of the Moiré Effect in a Volumetric Cube. Part II: Edge and Vertex Views. *J Applied Surf Sci,* 4(3), 01-24.

Abstract

In this paper, we continue investigating the moiré effect in a multilayered volumetric cube in detail. We calibrated the two views (edge and vertex). The corridors appear at angles with rational tangents modified by square roots of integers. The edge view resembles the face (front) view, whereas the vertex view is distinct. We derive formulas for the focus points in both views. Non-radial corridors in the vertex view comprise a series of equilateral triangles that run parallel and perpendicular to radial corridors. Formulas and illustrations are provided. These results can be used in crystallography and to minimize the moiré effect in volumetric 3D LED displays.

Keywords: Moiré Effect, Volumetric 3D Structure, Rational Tangents, 3D Moiré, Volumetric Moiré, LED-Based Volumetric 3D Displays

1. Introduction

The moiré effect occurs in layers of periodic structures (grids, lattices) viewed in transmission, where alternating dark and light regions appear. The effect is primarily considered in coplanar layers [1,2]. The moiré effect is relatively rare in three dimensions particularly in in measurements of three-dimensional (3D) objects [3-9]. We consider the moiré effect in a volumetric display with static voxels (small-radius spheres) at fixed locations of a simple cubic lattice [10,11]. In the simulation, we use the view images from a virtual camera; see Figure 1.

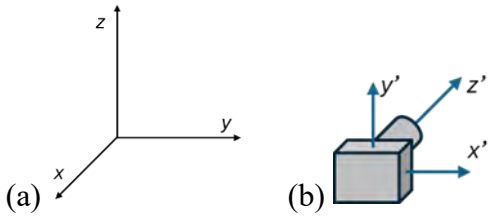


Figure 1: (a) Global System. (b) Local Camera System

We consider views along exact directions. Namely, three views perpendicular to the planes with the Miller indices (100), (110), and (111); see References [12-14]. The views are: the face (front) view when the local camera axis *z'* ("main" longitudinal axis) is directed along the crystallographic direction [100], the edge view (along [110]), and the vertex view (along [111]), as shown in Figure 2. The local camera axis *z'* is directed to the center of the cube. To illustrate the absence of roll (rotation around the longitudinal axis), Figure 2 shows the local camera axes as arrows.

The Euler angles (α, β, γ) corresponding to the face, edge, and vertex views are: (0, 0, 0), (arctan (1), 0, 0)) = (45°, 0, 0), and (arctan (1), -arctan ($\sqrt{2}/2$), 0) = (45°, -35.3°, 0). Note that the local camera axis *x'* is always horizontal.

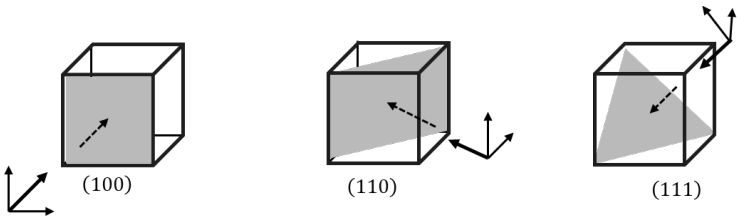


Figure 2: Views and Crystallographic Planes. (a) Face (100), (b) Edge (110), (c) Vertex (111). Arrows Show the Virtual Camera's Local Axes

Figures 3(a)-(c) show the three views with contours of the cube artificially drawn over view images. However, some lines coincide in these contours; therefore, for graphical clarity, Figure 3(d) shows sketches from a Slightly Deviated Perspectives directions.

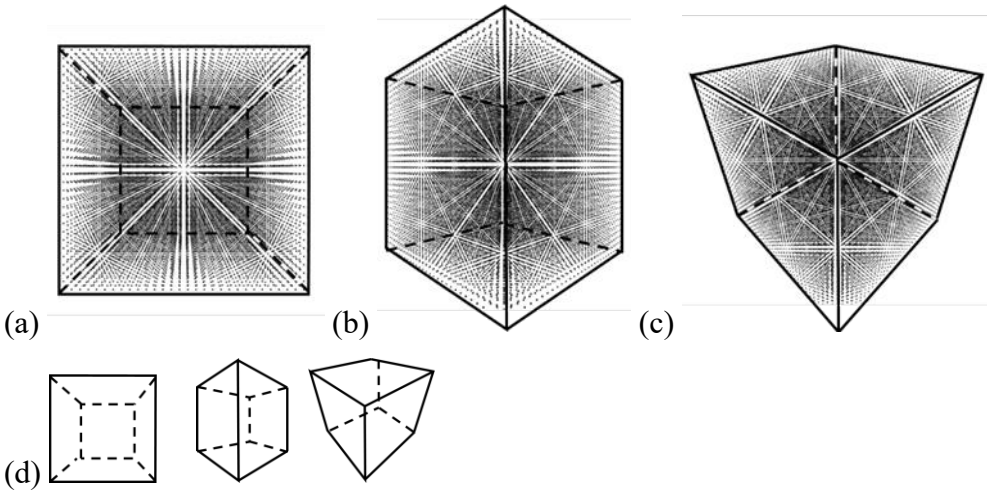


Figure 3: Three Views of the Volumetric Cube: (a) Face [100], (b) Edge [110], (c) Vertex [111], (d) Schematic Sketches from a Slightly Deviated Perspective

In the current Part II, we investigate the edge and vertex views of the volumetric cube, while Part I investigated the face view [15].

In volumetric displays moiré corridors may distract the observer's attention from the useful displayed 3D structure. Therefore, we should reduce this undesirable effect in 3D displays [16,17].

2. Materials and Methods

2.1. Calibration

We calibrated the edge and vertex views in ATU similarly to the face view (Part I [15]); see Appendix A. Figures 4 and 5 show the calibrated views.

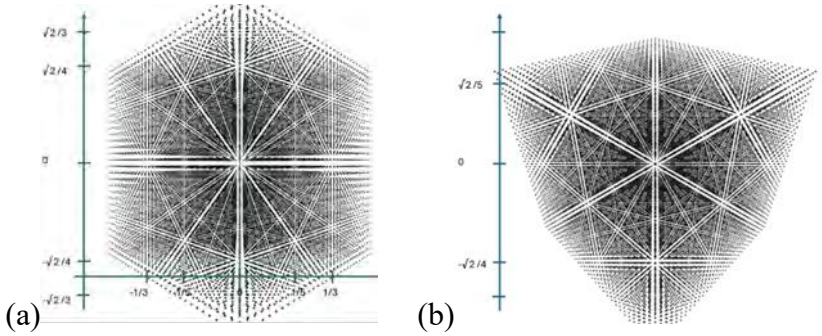


Figure 4: Calibrated Views: (a) Edge and (b) Vertex

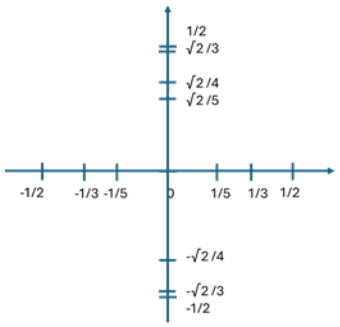


Figure 5: Axes Calibrated in Three Views

Note that we calibrated the vertex view only in the vertical direction. Nevertheless, the calibrated values (including intermediate ones) can be transferred to other axes and applied to any view and any direction, including the polar radius. The *y*-axis values containing √2 were taken from the calibration of the edge and vertex views.

2.2. Coordinate System

We use the orthogonal Cartesian system (*x, y*) and the polar system (*r, φ*), see Figure 6. The origin of the view image lies on the camera axis [18,19]. We also use the angle *θ* from the camera axis, as in the spherical system [20].

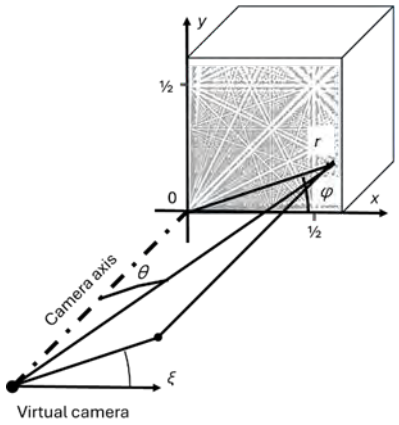


Figure 6: Coordinate Systems

3. Results

3.1. Edge View

3.1.1. Structure of Corridors

Figure 7 shows the edge view with calibrated units.

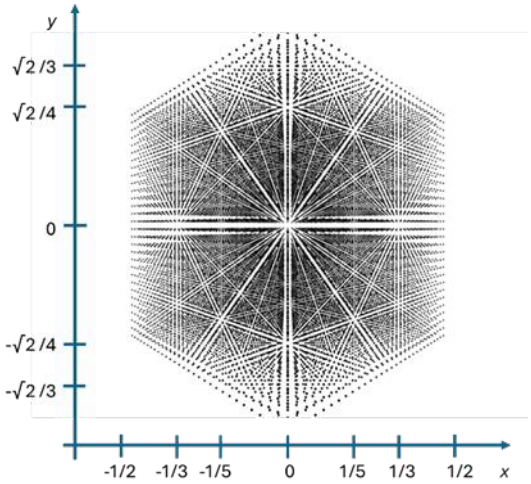


Figure 7: Edge View of the Cube of Voxels with Calibrated Axes

Figure 8 shows some (widest) radial corridors in the First Quadrant of the edge view.

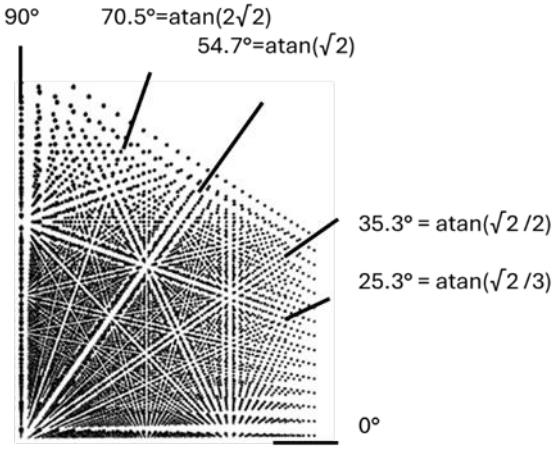


Figure 8: Radial Corridors of Edge View (First Quadrant)

3.1.2. Corridors

The corridor structure in the edge view is similar to that in the face view. We identified the corridors similarly to the face view: using Radon/Hough transforms, calibration, and visual inspection [21-24]. Table 1 lists the angles of the radial corridors observed in the edge view. Mutually perpendicular corridors (inclined perpendiculars) are highlighted in bold,

As in the face view parallel and perpendicular corridors to the radial rays exist; however, we did not observe all of them in practice [15].

p	0	1	1	**1**	**1**	2	**1**	**3**	**2**	**3**	4	5	
q		5	4	**3**	**2**	3	**1**	**2**	**1**	**1**	1	1	0
tan φ			$\frac{\sqrt{2}}{4}$	$\frac{\sqrt{2}}{3}$	$\frac{\sqrt{2}}{2}$	$\frac{2\sqrt{2}}{3}$	$\sqrt{2}$	$\frac{3\sqrt{2}}{2}$	$2\sqrt{2}$	$3\sqrt{2}$	$4\sqrt{2}$	$5\sqrt{2}$	
	0	**0.24**	**0.35**	**0.47**	**0.71**	0.94	1.41	2.12	2.83	4.24	5.66	7.07	∞
φ	0	13.26	19.47	25.24	35.26	43.31	54.74	64.76	70.53	76.74	79.98	81.95	90
Inverse	-∞	-4.24	-2.83	-2.12	-1.41	-1.06	**-0.71**	**-0.47**	**-0.35**	-0.24	-0.18	-0.14	**0**
negative			-√2/2	-√2/2	-√2/2	-3√2/4	**-√2/2**	**-√2/3**	**-√2/4**	-√2/6	-√2/8	-√2/10	

Table 1: Radial Corridors in Edge View

Note the values 0.71 and 1.41 (which have the same absolute value but opposite signs), located at the corners of the square surrounding the 43.31° angle, similarly to the radial corridors in the face view around the angle 45° [15].

The angles of the radial corridors have tangents equal to rational numbers multiplied by √2,

$$\varphi = \tan^{-1}\frac{p}{q}\sqrt{2} \qquad (1)$$

where p, q are integers 0, 1, 2, 3, …
This formula shows that the corridors contract toward the vertical axis (ordinate). Note that the polar angle is measured from the abscissa.

3.1.3. Focus Points

As in the face view, horizontal, vertical, and inclined lines intersect at "focus" points on the x- and y-axes. Tables 2 and 3 list the focus points.

m_x	0	1	1	1	1	3	1	3	2	3	4	5
n_x	1	7	5	3	2	5	1	2	1	1	1	1
$X(\pm)$		$\frac{\sqrt{2}}{7}$	$\frac{\sqrt{2}}{5}$	$\frac{\sqrt{2}}{3}$	$\frac{\sqrt{2}}{2}$	$\frac{3\sqrt{2}}{5}$	$\sqrt{2}$	$\frac{3\sqrt{2}}{2}$	$2\sqrt{2}$	$3\sqrt{2}$	$4\sqrt{2}$	$5\sqrt{2}$
	0.00	0.20	0.28	0.47	0.71	0.85	1.41	2.12	2.83	4.24	5.66	7.07

Table 2: Focus Points in Edge View on the Abscissa

m_y	0	1	1	1	1	1	1	3	1
n_y		10	8	6	5	4	3	8	2
$Y(\pm)$		$\frac{\sqrt{2}}{10}$	$\frac{\sqrt{2}}{8}$	$\frac{\sqrt{2}}{6}$	$\frac{\sqrt{2}}{5}$	$\frac{\sqrt{2}}{4}$	$\frac{\sqrt{2}}{3}$	$\frac{3\sqrt{2}}{8}$	$\frac{\sqrt{2}}{2}$
	0.00	0.14	0.18	0.24	0.28	0.35	0.47	0.53	0.71

Table 3: Focus Points in Edge View on the Ordinate

The radial angles mostly have small $p, q \leq 3$, while other angles may have larger $m, n \geq 4$. However, we did not observe all combinations of m_x/n_x, m_y/n_y.

3.2. Vertex View

3.2.1. Structure of Corridors

Figures 9 and 10 show the vertex view with calibrated units and the wide corridors.

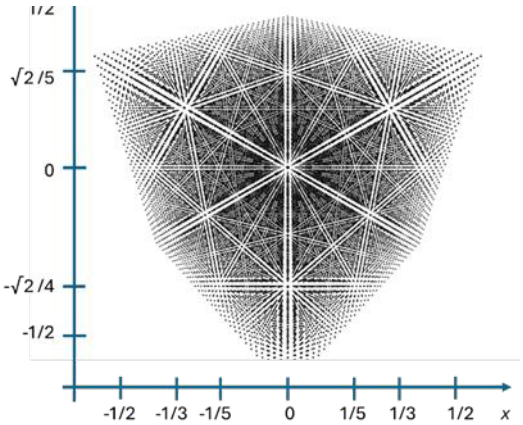


Figure 9: Vertex View of the Cube of Voxels with Calibrated Axes

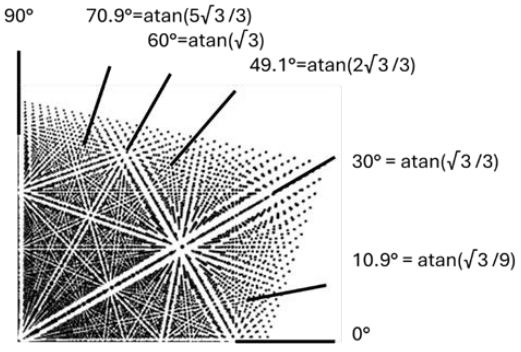


Figure 10: Widest Radial Corridors in the First Quadrant

3.2.2. Corridors

The polar angles of the radial corridors have tangents derived from rational numbers,

$$\varphi = \tan^{-1}\frac{p}{q}\sqrt{3} \qquad (2)$$

m	0	1	1	2	1	5	
n		9	3	3	1	3	0
tan φ		$\frac{\sqrt{3}}{9}$	$\frac{\sqrt{3}}{3}$	$\frac{2\sqrt{3}}{3}$	$\sqrt{3}$	$\frac{5\sqrt{3}}{3}$	
	0	0.19	**0.58**	1.15	1.73	2.89	∞
φ	0	10.89	30.00	49.11	60.00	70.89	90
Inverse	-∞	-5.20	-1.73	-0.87	**-0.58**	-0.35	0
negative		-3√3	-√3	-√3/2	**-√3/3**	-√3/5	

Table 4: Radial Corridors in Vertex View

Two angles are exactly equal to 30° and 60°. These angles create the triangular symmetry [20].

Note the values 0.58 and 1.73 (with the same absolute value but opposite signs), located at the corners of the square surrounding the 49.11° angle, similarly to the Table 1

There are "focus" points on the x- and y-axes with intersecting horizontal and inclined lines. However, the vertex view has no vertical corridors except for the ordinate. Table 6 is technically divided into 2 parts (for negative and positive y).

3.2.3. Focus Points

m_x	0	1	1	1	1	1	1
n_x	1	12	9	6	5	3	2
X (±)	0	$\frac{\sqrt{3}}{12}$	$\frac{\sqrt{3}}{9}$	$\frac{\sqrt{3}}{6}$	$\frac{\sqrt{3}}{5}$	$\frac{\sqrt{3}}{3}$	$\frac{\sqrt{3}}{2}$
	0.00	0.14	0.19	0.29	0.35	0.58	0.87

Table 5: Focus Points in Vertex View on the Abscissa

m_y	-1	-2	-1	**-1**	-2	-1	-1	-1	…
n_y	1	5	3	**4**	11	7	10	13	…
Y (<0)	$-\sqrt{2}$	$-\frac{2\sqrt{2}}{5}$	$-\frac{\sqrt{2}}{3}$	$-\frac{\sqrt{2}}{\mathbf{4}}$	$-\frac{2\sqrt{2}}{11}$	$-\frac{\sqrt{2}}{7}$	$-\frac{\sqrt{2}}{10}$	$-\frac{\sqrt{2}}{13}$	
	-1.41	-0.57	-0.47	**-0.35**	-0.26	-0.20	-0.14	-0.11	

Table 6: Focus Points in Vertex View on the Ordinate. (*to be Continued Below*)

m_y	…		1	1	1	**1**	1	2	1	1	2
n_y	…	**0**	11	8	7	**5**	4	7	3	2	1
Y (≥0)		**0**	$\frac{\sqrt{2}}{11}$	$\frac{\sqrt{2}}{8}$	$\frac{\sqrt{2}}{7}$	$\frac{\sqrt{\mathbf{2}}}{\mathbf{5}}$	$\frac{\sqrt{2}}{4}$	$\frac{2\sqrt{2}}{7}$	$\frac{\sqrt{2}}{3}$	$\frac{\sqrt{2}}{2}$	$2\sqrt{2}$
		0.0	0.13	0.18	0.20	**0.28**	0.35	0.40	0.47	0.71	2.83

Table 6: (continued). Focus Points in Vertex View on the Ordinate

3.2.4. Triangles

The non-radial corridors comprise equilateral triangles centered at the origin. Figure 11 shows triangles symmetric with respect to the *y*-axis, with bases parallel to the abscissa. Appendix B gives more examples. These triangles come in sizes in the ratios 1:2 and 4:5. An up-triangle is inscribed in a down-triangle, and vice versa.

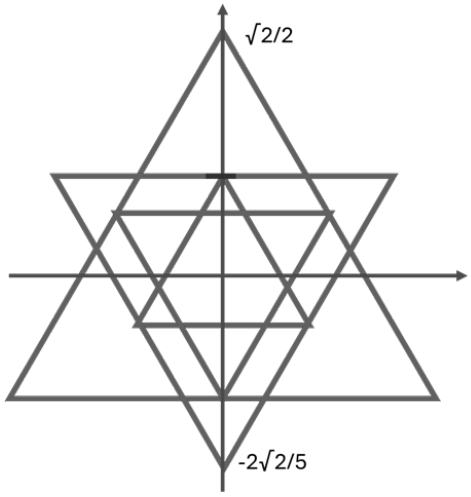


Figure 11: Symmetric Triangles

The sides of the up-triangles are perpendicular to the rays -90°, 30°, and -30°, and the sides of the down-triangles are perpendicular to 90°, 30°, and -30°. Based on calibration, the side of the triangle is

$$a = s\frac{\sqrt{6}}{t} \quad (3)$$

where

$$t = 3 + 2^i \quad (4)$$

$i = 0, 1$ and $s = 1, 2$; so, the triangle can be twice as large, depending on s.

There are also several pairs of asymmetric triangles (centered at the origin too) with their bases inclined from the abscissa (and extensions of their sides) [20]. Figure 12 shows some observed asymmetric triangles. More examples can be found in Appendix B.

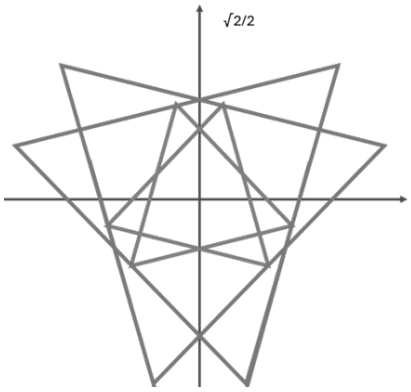


Figure 12: Asymmetric Triangles with the Base Angle 14°

Note that the up-triangle is inscribed in the down-triangle and vice versa, so their sides are in the ratio 1:2.

The side of such a triangle (basic 1):

$$a_\gamma = s\frac{t-3}{\sqrt{t^2+3}}\sqrt{6} = s\frac{2^{i-1}\sqrt{6}}{\sqrt{2^{2i-2}+3*2^{i-1}+3}} \quad (5)$$

where s = 1/2, 1, 2, so triangles can be twice as small or large (symbolically; 0.5x, 1x, and 2x). No up-triangles (1x) were observed, but down-triangles (0.5x and 2x) were noted.

The inclination angle of the base of the asymmetric triangles is

$$\gamma = \tan^{-1}\frac{\sqrt{3}}{t} = \tan^{-1}\frac{\sqrt{3}}{3+2^i} \quad (6)$$

where t is the same function as in Equation (4), but i = 0, 1, 2, 3.

When $i \to \infty$,

$$\lim_{i\to\infty} a_\gamma = \lim_{i\to\infty} s\frac{2^{i-1}\sqrt{6}}{\sqrt{2^{2i-2}+3*2^{i-1}+3}} = s\frac{2^{i-1}\sqrt{6}}{2^{i-1}} = s\sqrt{6} \quad (7)$$

$$\lim_{i\to\infty}\gamma = \lim_{i\to\infty}\tan^{-1}\frac{\sqrt{3}}{3+2^i} = 0 \quad (8)$$

Comparing formulas for the side and focus points (Appendix C), one may conclude that the symmetric triangles with γ = 0 can be considered as a limiting case of asymmetric ones, although with different s.

Other parameters of asymmetric and symmetric triangles (lines of intersection of their sides) on the y-axis can be obtained analytically from formulas for the side and the base angle [20]. For instance, the angle between the side and the ordinate:

$$\sin\gamma = \frac{t-3}{2\sqrt{t^2+3}} = \frac{2^{i-2}}{\sqrt{2^{2i-1}+3*2^{i-1}+3}} \quad (9)$$

The focus points are:

$$y_{FAR} = s\sqrt{2} \quad (10)$$

$$y_{NEAR} = s\frac{t-3}{t}\frac{1}{\sqrt{2}} = s\frac{2^{i-1}}{2^i+3}\sqrt{2} \quad (11)$$

$$y_{MID} = s\frac{t-3}{t+3}\sqrt{2} = s\frac{2^i}{2^i+6}\sqrt{2} \quad (12)$$

For symmetric triangles, the mid focus coincides with the far focus, and the near focus is half the far focus because the base angle is zero. Note that for asymmetric triangles, the near focus of the down-triangle is equal to the mid focus of the up-triangle with the next i.

The ratios of the far focus point and near and mid focus points (for i = 0, …,3) are

$$\frac{y_{FAR}}{y_{FAR}} = 8, 5, \frac{7}{2}, \frac{11}{4} \quad (13)$$

$$\frac{y_{FAR}}{y_{MID}} = 7,\ \ 4, \frac{5}{2}, \frac{7}{4} \quad (14)$$

Appendix C provides numerical values. Appendix D provides numerical values and formulas for the distances from the origin.

Figure 13 shows some symmetric triangles and asymmetric triangles with positive and negative focus points. Appendix B gives more examples. Note how they cross the symmetric triangles in the middle of their sides and touch their vertices.

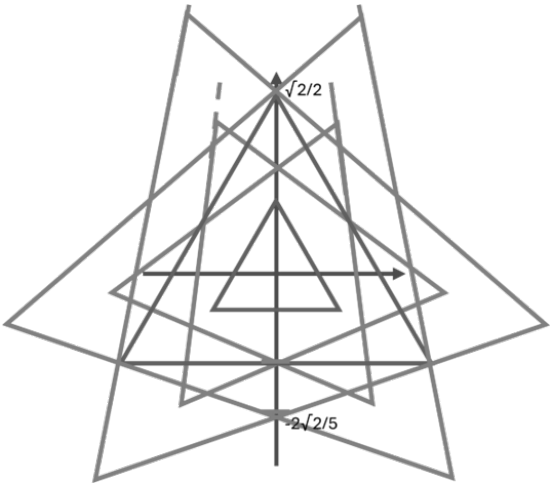
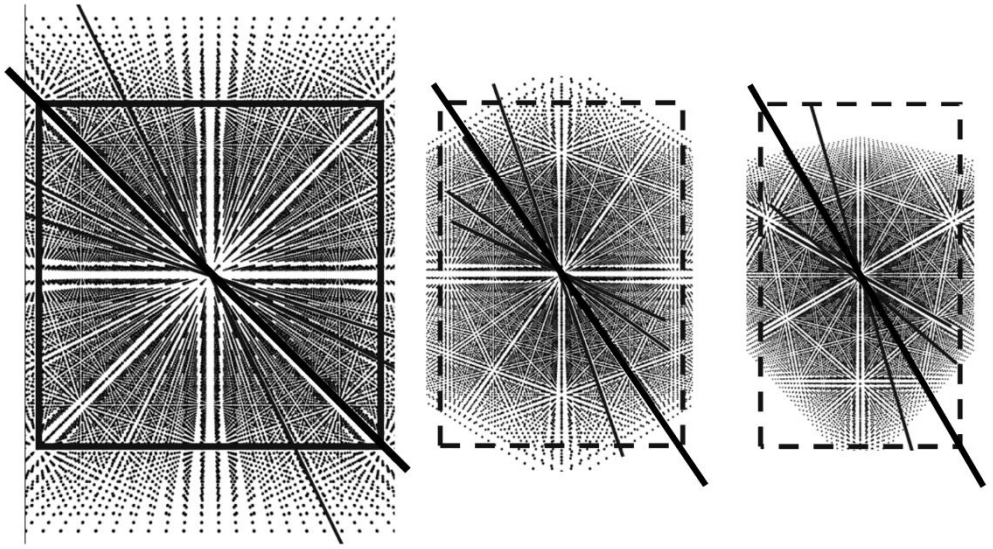


Figure 13: Symmetric and Asymmetric Triangles

4. Discussion

Figure 14 shows the corresponding corridors in the three views.

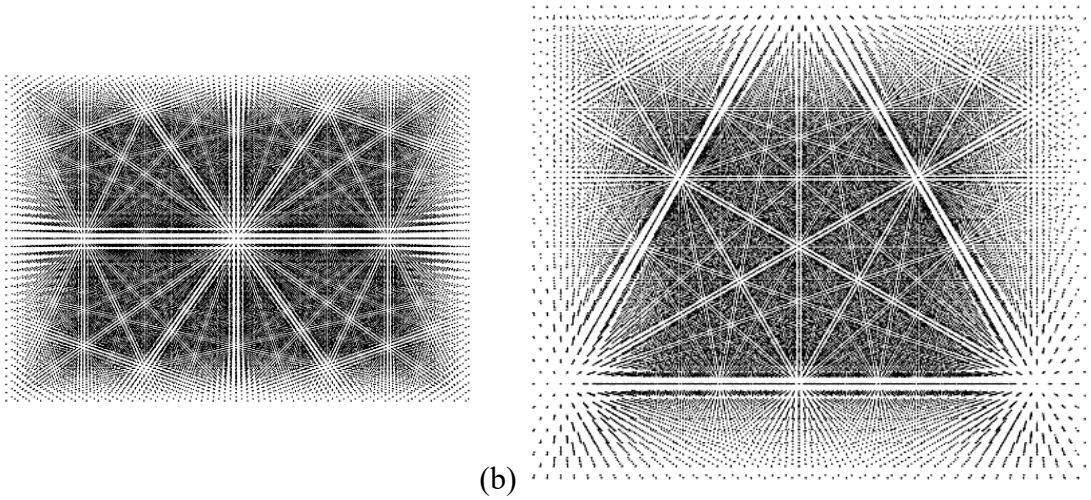


(a) (b) (c)

Figure 14: (a) Face View Corridor Arctan (1/2) and Some of its Neighbors Transformed to other Views: (b) Edge View, (c) Vertex View

The moiré effect in cubic configurations can be modeled as a parallelepiped that preserves the viewing direction but features an alternative arrangement (a rectangular parallelepiped is always positioned perpendicular to the camera axis), as suggested in [25]. Specifically, when viewed from the face, the layers remain unchanged (i.e., they form a square lattice with side length a), and the interplanar spacing is a. However, to simulate the edge view in the parallelepiped, each layer is characterized by an aspect ratio of $\sqrt{2}$, and alternating pairs of layers (with phase shifts of 0 and π) have an interplanar spacing of $a/\sqrt{2}$. Similarly, to simulate the vertex view, each layer forms a triangular lattice with side length $a\sqrt{2}$, and alternating triplets of layers (with phase shifts of 0, $\pi/3$, and $2\pi/3$) have an interplanar spacing of $a/\sqrt{3}$.

Figure 15 presents simulation results for two viewpoints within the framework of an alternative configuration; compare the images below with the corresponding images from Sections 3.1 and 3.2.



(a) (b)

Figure 15: Moiré Corridors of the Two Cameras Obtained in the Alternative Layer Layouts. Reproduced from the digital PDF version of [25] Under the Terms of the Creative Commons Attribution-Non-Commercial 4.0 License (CC BY-NC 4.0)

The main corridors observed in the basic layout in the same object but different camera axes (shown in Figures 7 and 9) and in the alternative layouts (the parallelepiped with different layers but the same camera) are practically identical. The few differences are not significant [25].

5. Conclusion

We investigated the moiré effect in the multilayered cubic lattice observed from a finite distance along the [001], [110], and [111] directions and found the moiré corridors. The illustrations show the crystallographic planes. We calibrated the edge and vertex views in angular units and derived formulas for corridor angles and axial focus points. The edge view is mostly similar to the face view, but the vertex view differs significantly. We identified several series of symmetric and asymmetric triangles (arranged in pairs). We derived formulas for triangles (sizes, distances, base angles, and far/near focus points) accompanied by multiple illustrations. As with moiré angles in barrier displays, the characteristic angles of moiré corridors in a simple cubic lattice (edge and vertex cameras) have rational tangents modified by square roots of integers. This study provides direct observation of crystallographic planes, which may be useful for crystallography. These conditions can minimize the moiré effect in volumetric displays with fixed voxel positions, such as static LEDs.

References

1. Amidror, I. (2009). *The Theory of the Moiré Phenomenon: Volume I: Periodic Layers*. Springer.
2. Bryngdahl, O. (1974). Moiré: formation and interpretation. Journal of the Optical Society of America, 64(10), 1287-1294.
3. Creath, K., & Wyant, J. C. (1992). Moiré and fringe projection techniques. *Optical shop testing,* 653-685.
4. Saveljev, V. (2022 *The Geometry of the Moiré Effect in One, Two, and Three Dimensions*. Cambridge Scholars Publishing.
5. Theocaris, P. S. (1967). Moiré topography of curved surfaces: the moiré method is extended to measure deflections and slopes in cylindrical and conical shells. *Experimental Mechanics, 7(*7), 289-296.
6. Sciammarella, C. A. (1982). The moiré method—a review: The main developments in the area of moiré as a tool to measure displacements, contours, slopes and strains are reviewed and some typical applications are shown. *Experimental mechanics, 22*(11), 418-433.
7. Chiang, F. P. (1979). Moiré methods of strain analysis. *Experimental mechanics, 19*(8), 290-308.
8. Patorski, K., Kujawińska, M. (1993). *Handbook of the moiré fringe technique.*Elsevier.
9. Post, D., Han, B., & Ifju, P. (1997). *High sensitivity moiré: experimental analysis for mechanics and materials.* Springer.
10. Weisstein, E.W. (2025). Cubic lattice. *From MathWorld--A Wolfram Resource.*
11. Visual physics and mathematics/Crystal structures. (2024, February 1). *Wikibooks.* Retrieved October 2, 2026.
12. Monaco, H. L., Viterbo, D., Scordari, F., Gilli, G., Zanotti, G., & Catti, M. (2002). Fundamentals of crystallography. C. Giacovazzo (Ed.). Oxford: Oxford university press.
13. Ashcroft, N. W., & Mermin, N. D. (1976). *Solid state physics.* Holt, Rinehart and Winston.
14. Popov, I., & Besley, E. (2026). Three-dimensional moiré crystallography. *arXiv preprint arXiv:2601.04971.*
15. Saveljev, V. (2026). Simulation of the Moiré Effect in a Volumetric Cube. Part I: Face View. *J Applied Surf Sci, 4*(3), 01-16.
16. Pimenta, W., & Santos, L. P. (2012). A comprehensive taxonomy for three-dimensional displays. *WSCG'2012* (pp. 139-146).
17. Blundell, B. G., & Schwarz, A. J. (2002). The classification of volumetric display systems: characteristics and predictability of the image space. *IEEE Transactions on Visualization and Computer Graphics, 8*(1), 66-75.

18. Hartley, R., & Zisserman, A. (2003). *Multiple view geometry in computer vision*. Cambridge: Cambridge university press.
19. Willson, R. G., & Shafer, S. A. (1994). What is the center of the image?. *Journal of the Optical Society of America A, 11*(11), 2946-2955.
20. Saveljev, V. (2023). Moiré effect in multilayered 3D lattice. *Applied Optics, 62*(11), 2792-2799.
21. Aramini, R., Delbary, F., Beltrametti, M. C., Piana, M., & Massone, A. M. (2016). The Radon transform and the Hough transform: a unifying perspective. *arXiv preprint arXiv:1605.09201*.
22. van Ginkel, M., Hendriks, C. L., & van Vliet, L. J. (2004). A short introduction to the Radon and Hough transforms and how they relate to each other. Delft University of Technology.
23. Ballard, D. H. (1981). Generalizing the Hough transform to detect arbitrary shapes. *Pattern recognition, 13*(2), 111-122.
24. Toft, P. A. (1996, May). Using the generalized Radon transform for detection of curves in noisy images. In 1996 *IEEE International Conference on Acoustics, Speech, and Signal Processing Conference Proceedings* (Vol. 4, pp. 2219-2222). IEEE.
25. Saveljev, V. (2026). Combined Physical and Computational Simulation of the Moiré Effect in 3D Objects and Displays. In *Intelligent Systems: From Data to Decisions* (Ch. 5, pp. 93-122). Haliç Publishing House, İstanbul, Türkiye.

Appendix A: Calibration

A1. Calibration of the Edge View

A1.1. Horizontal Angles

Consider a layer parallel to the horizontal plane (001) viewed from the direction slightly deviated from [100]; see Figure A1.

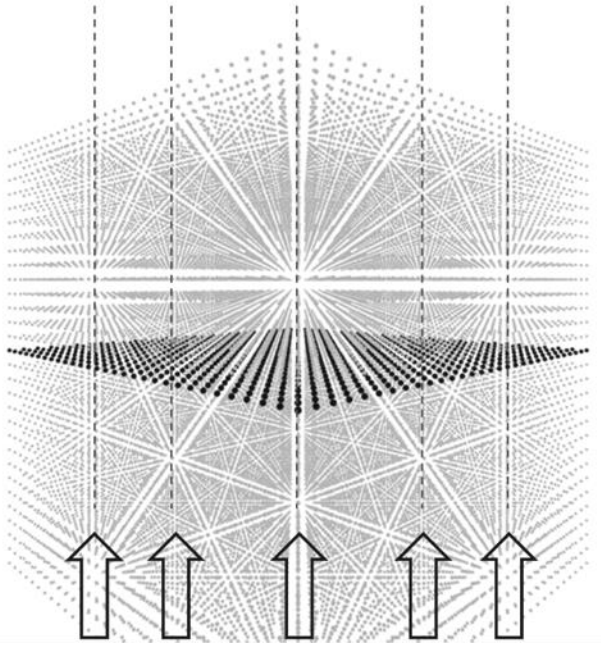


Figure A1: Plane (001) in Cube

One corridor is clearly visible in the middle, with two pairs of symmetric lateral corridors. Figure A2 shows the grid lines and voxel connections in the lateral corridors.

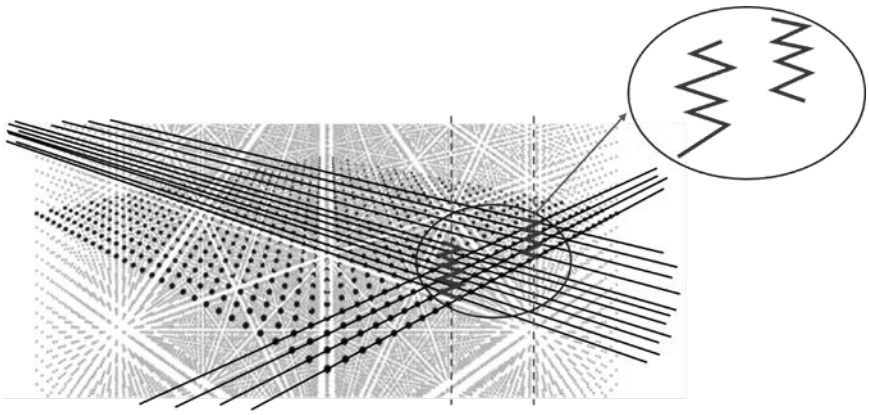


Figure A2: Plane (001) with a Grid of Voxels

Figure A3 shows the voxel grid on this plane in the [100] direction. The voxel counts for each leg are shown on the right.

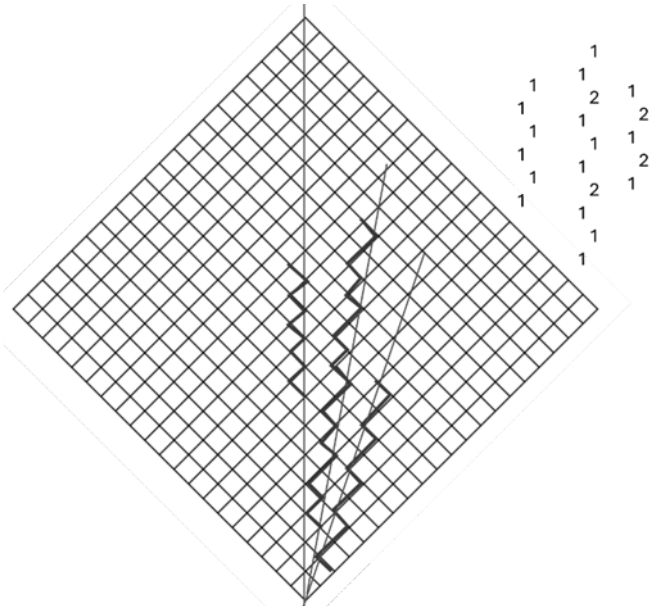


Figure A3: Plane (001) with Corridors

Counting voxels along zigzag lines gives the angles of the corridors from the axis: atan(1/5) and arctan (1/3).

A1.2. Vertical Angles

Consider the vertical diagonal plane $(1\bar{1}0)$ observed from the edge, as shown in Figure A4.

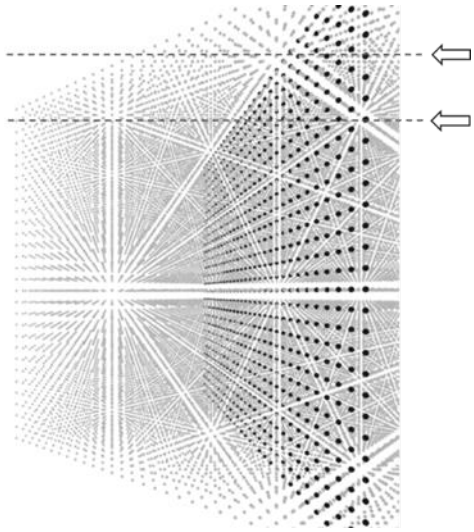


Figure A4: Plane $(1\bar{1}0)$ in Cube

The clearly visible corridors are in the middle, with two pairs of symmetric lateral ones above and below.

Connections of voxels in lateral corridors are shown in Figure A5.

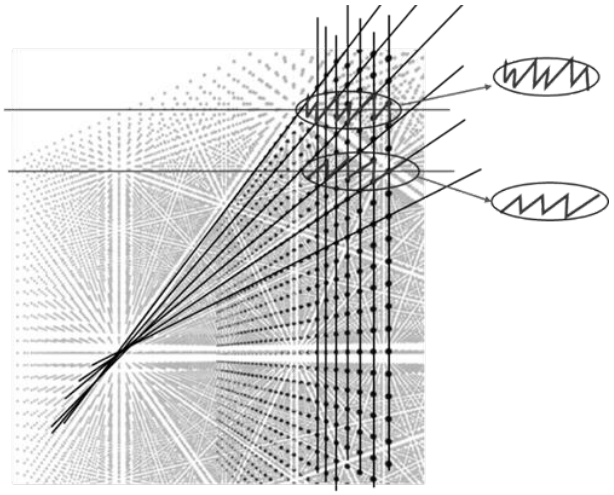


Figure A5: Plane $(1\bar{1}0)$ with a Grid of Voxels

Figure A6 shows the voxel grid from a direction $[1\bar{1}0]$ perpendicular to the diagonal plane. The voxel counts along the zigzag lines are shown on the right side.

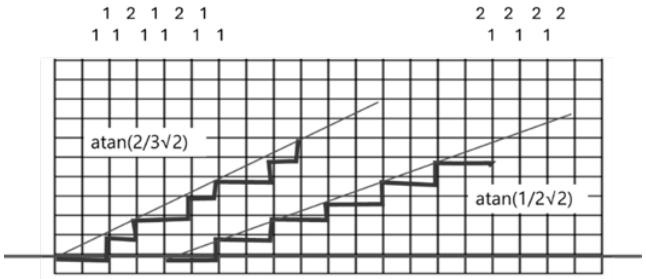


Figure A6: Plane $(1\bar{1}0)$ with Corridors

The voxel counts show that the angles of the side vertical corridors are arctan(1/2√2) = arctan (√2/4) and arctan (2/3√2) = arctan (√2/3).

Figure A7 shows the edge view calibration result.

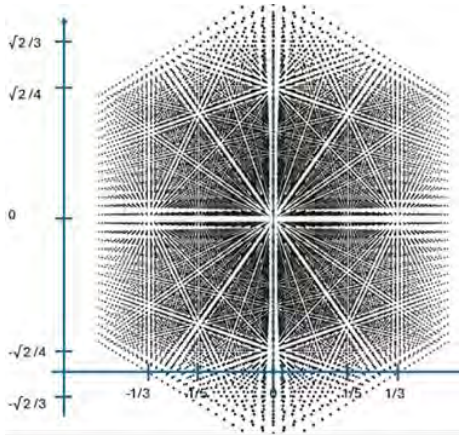


Figure A7: Edge View Calibrated in Arctangent Units (ATU)

A2. Calibration of the Vertex View

Consider the same plane $(1\bar{1}0)$ viewed from a different direction $[\bar{1}\bar{1}\bar{1}]$, see Figure A8.

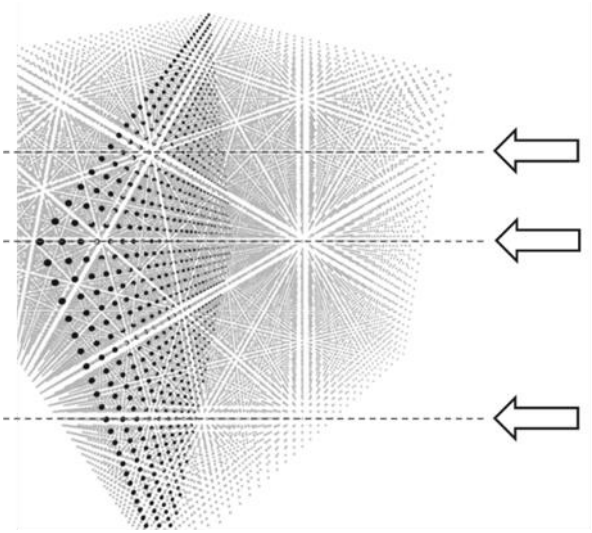


Figure A8: Plane (110) in Cube from Another Direction

Only vertical angles appear in this case. The clearly visible corridors are: one in the middle and two asymmetric corridors above and below it. Connection of voxels in asymmetric corridors is shown in Figure A9.

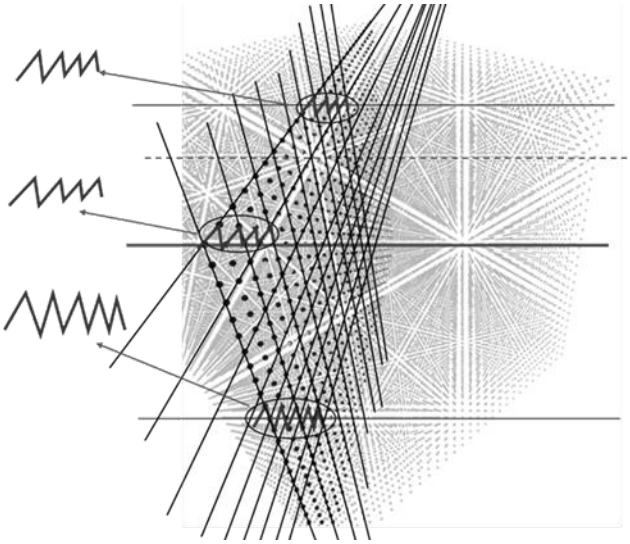


Figure A9: Plane $(1\bar{1}0)$ with Grid of Voxels

In the perpendicular view (direction $[1\bar{1}0]$), the voxel grid is shown in Figure A10. The angles of the side corridors are arctan $(1/(2\sqrt{2}))$ and arctan $(2/\sqrt{2})$.

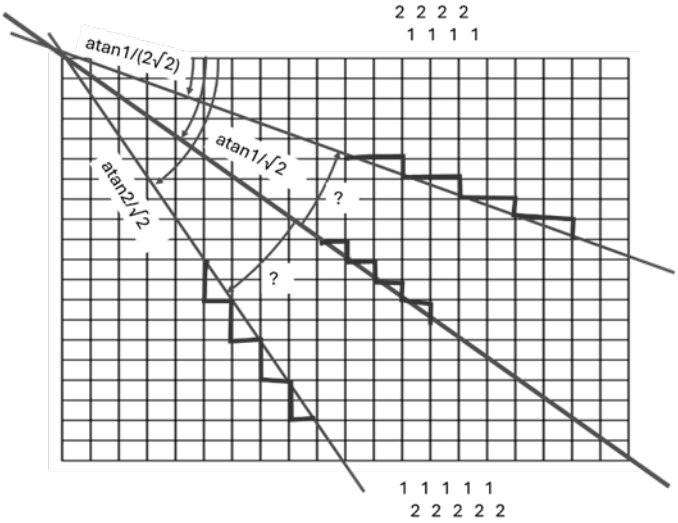


Figure A10: Plane $(1\bar{1}0)$ with Corridors

However, we need the differences from the camera axis at arctan $(1/\sqrt{2})$. The difference between arctangents is known from trigonometry; therefore,

$$\tan^{-1}\frac{1}{\sqrt{2}} - \tan^{-1}\frac{1}{2\sqrt{2}} = \tan^{-1}\frac{\frac{1}{\sqrt{2}} - \frac{1}{2\sqrt{2}}}{1 + \frac{1}{2\sqrt{2}}\frac{1}{\sqrt{2}}} = \tan^{-1}\left(\frac{2-1}{4+1}\sqrt{2}\right) = \tan^{-1}\frac{\sqrt{2}}{5} \qquad (A1)$$

$$\tan^{-1}\frac{1}{\sqrt{2}} - \tan^{-1}\frac{2}{\sqrt{2}} = \tan^{-1}\frac{\frac{1}{\sqrt{2}} - \frac{2}{\sqrt{2}}}{1 + \frac{1}{\sqrt{2}}\frac{2}{\sqrt{2}}} = \tan^{-1}\left(\frac{1-2}{2+2}\sqrt{2}\right) = -\tan^{-1}\frac{\sqrt{2}}{4} \qquad (A2)$$

Figure A11 shows the corridor locations and their angles.

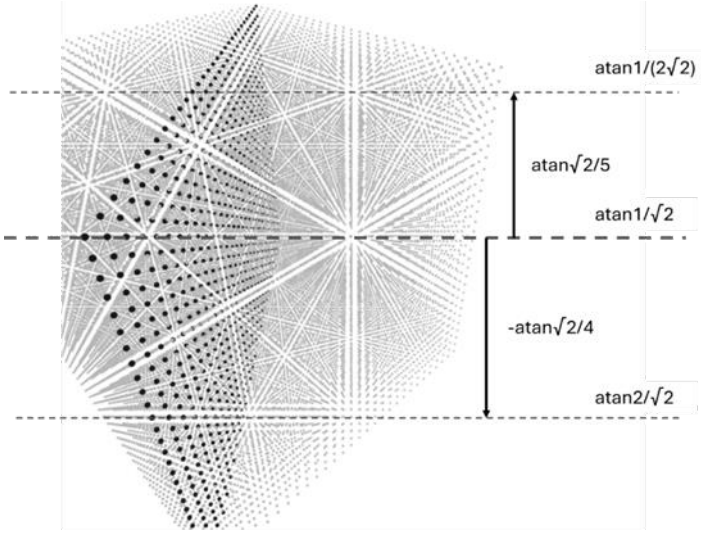


Figure A11: Plane $(1\bar{1}0)$ in Cube with Corridor Angles

Figure A12 shows the calibration results.

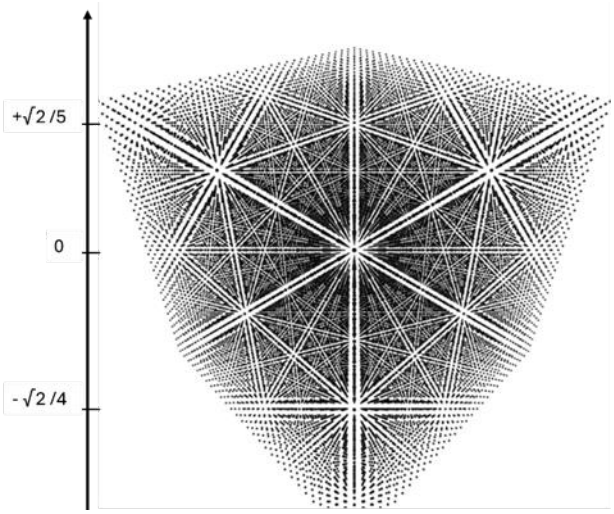


Figure A12: Vertex View Calibrated in Arctangent Units (ATU)

Appendix B: Detailed Images of Symmetric and Asymmetric Triangles in Vertex View

Figure B1 shows the symmetric triangles centered at the origin. Figures B2-B5 show pairs of asymmetric triangles (also centered at the origin), with their bases inclined from the abscissa by 9°-23° (and extensions of their sides). Figures B6 and B7 show asymmetric up-triangles; Figure B8 shows asymmetric down-triangles.

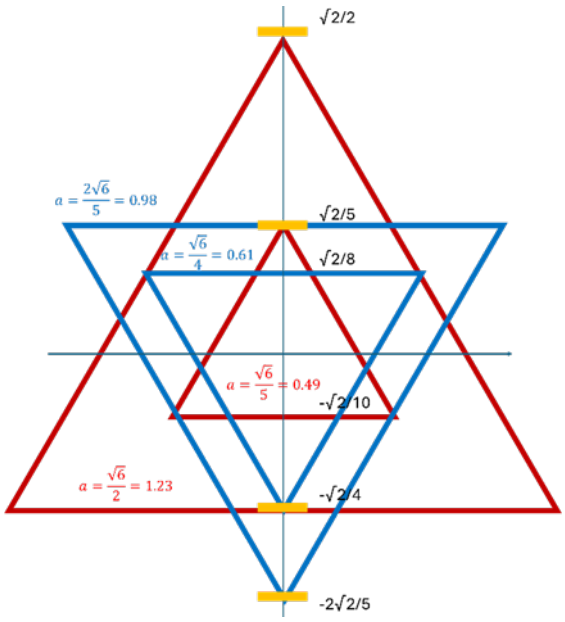


Figure B1: Symmetric Triangles with Bases Parallel to the Abscissa (angle 0°)

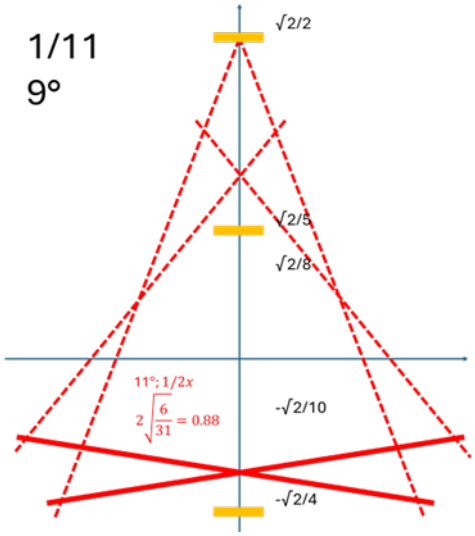


Figure B2: Asymmetric Triangles with Angle 9°

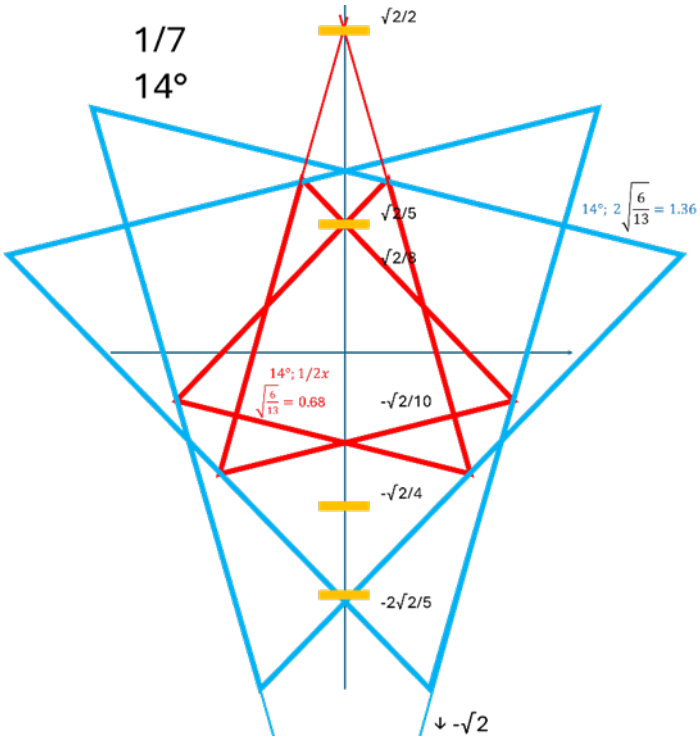


Figure B3: Asymmetric Triangles with Angle 14°

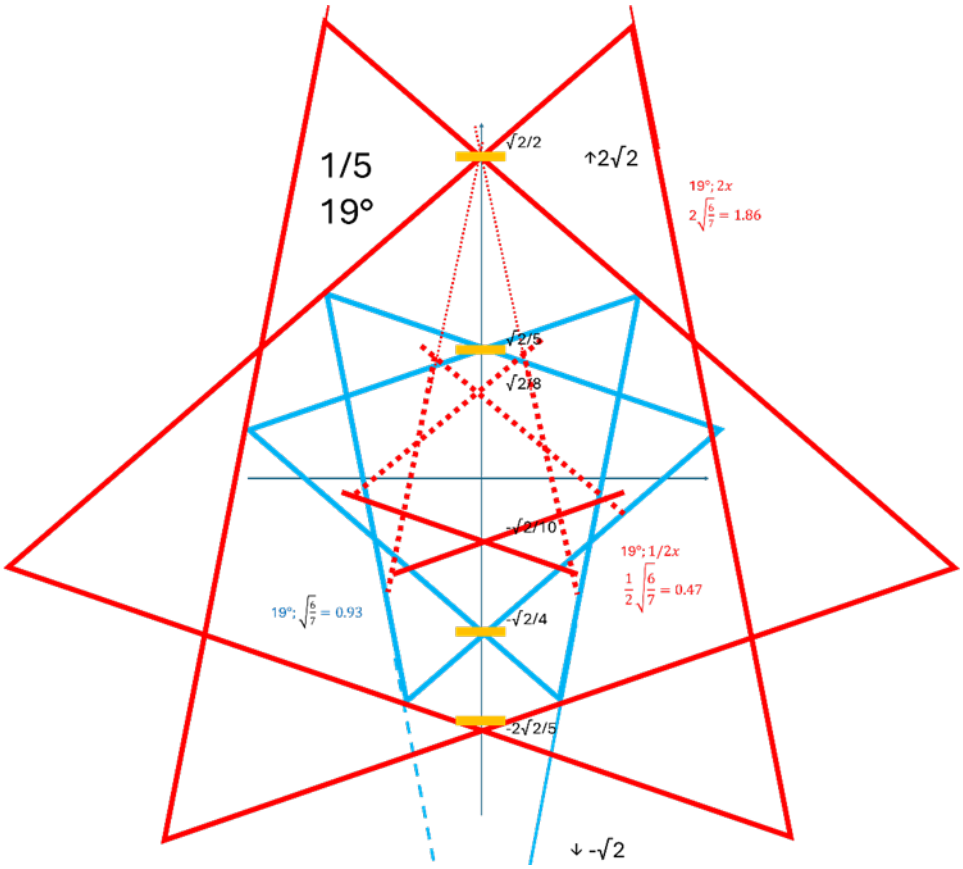


Figure B4: Asymmetric Triangles with Angle 19°

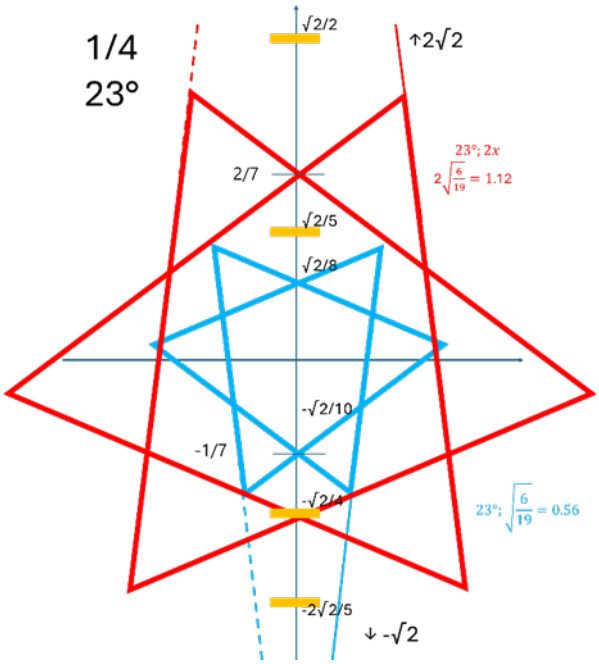


Figure B5: Asymmetric Triangles with Angle 23°

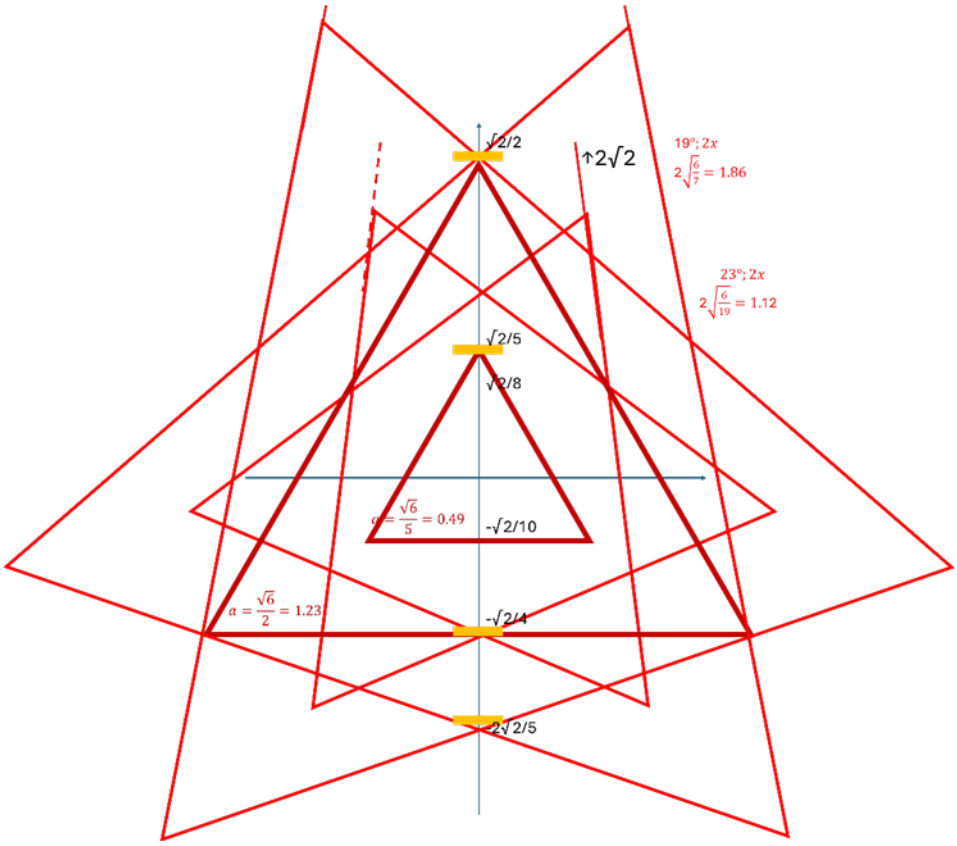


Figure B6: Asymmetric Up-Triangles with Positive Focus 2√2 (2x) and Symmetric Up-Triangles

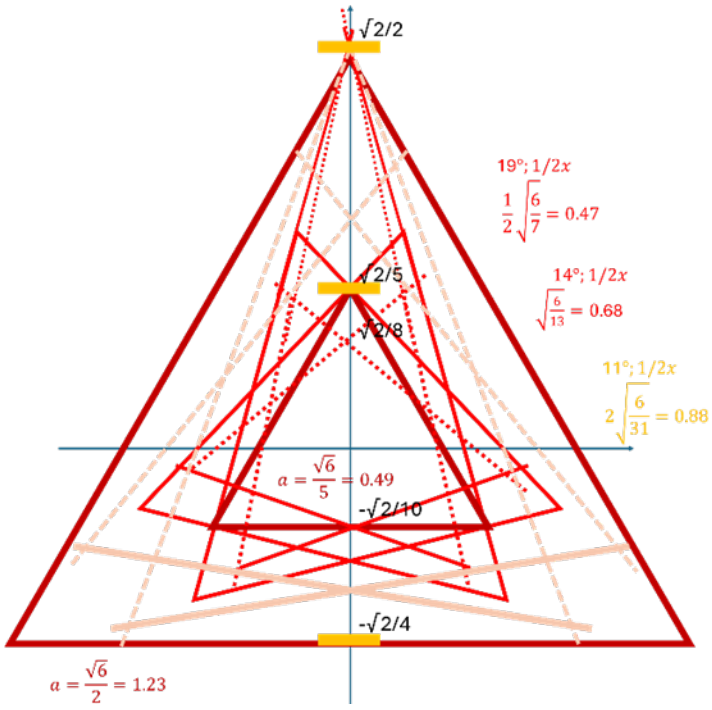


Figure B7: Asymmetric Up-Triangles with Positive Focus √2/2 (0.5x) and Symmetric Up-Triangles (Magnified)

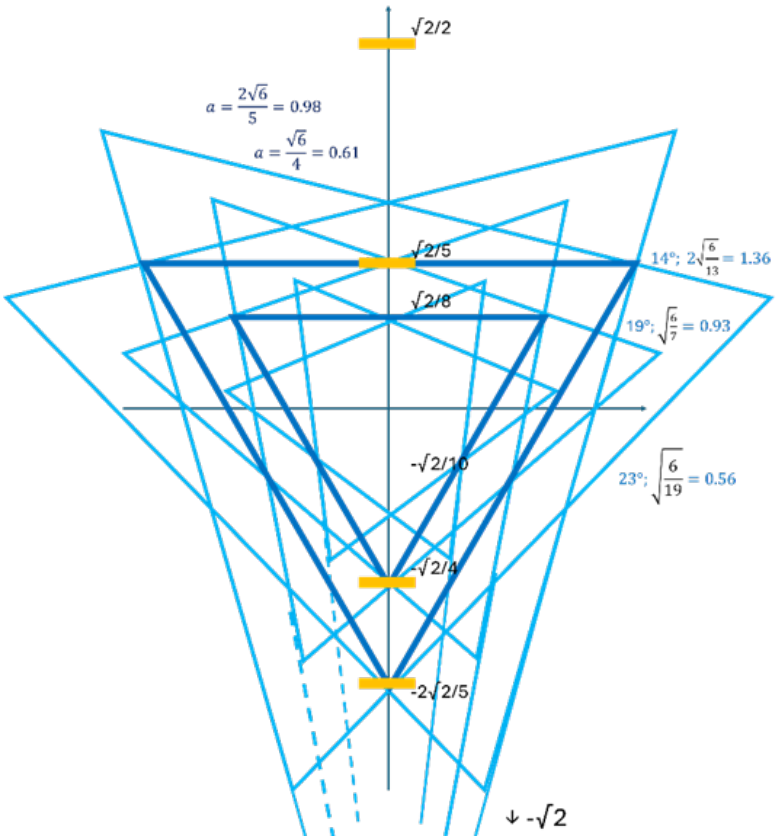


Figure B8: Asymmetric Down-Triangles with Negative Focus -√2 (all 1x) and Symmetric Up-Triangles

Appendix C: Numerical Characteristics of Triangles

Tables C1-C3 give the numerical values for symmetric triangles and asymmetric pairs of triangles, including the observed far focus point (an optional "basic" value is provided for calculations). Specifically, Table C1 contains the triangle side lengths. Tables C2-C4 contain the far, mid, and near focus-point values. The logically corresponding values are encircled. The numerical data were calculated using Equations (6), (10)-(12).

i	*t*	tan	*γ*	Basic	1x	2x	0.5x	1x	2x
					s=1	*s*=2	*s*=1/2	*s*=1	*s*=2
Asymmetric triangles					down (▼▼)		up (▲▲)		
0	4	$\frac{\sqrt{3}}{4}$	±23.4°	$\sqrt{\frac{6}{19}}$	0.56				1.12
1	5	$\frac{\sqrt{3}}{5}$	±19.1°	$\sqrt{\frac{6}{7}}$	0.93		0.47		1.86
2	7	$\frac{\sqrt{3}}{7}$	±13.9°	$2\sqrt{\frac{6}{13}}$	1.36		0.68		
3	11	$\frac{\sqrt{3}}{11}$	±8.9°	$4\sqrt{\frac{6}{31}}$			0.88		
∞			**0**	$\sqrt{6}$			**1.23**		
Symmetric triangles					down (▼)			up (▲)	
0	4		**0**	$\frac{\sqrt{6}}{4}$	0.61				**1.23**
1	5		**0**	$\frac{\sqrt{6}}{5}$		0.98		0.49	

Table C1: Sides of Triangles

i	*t*	Basic	1x	2x	0.5x	1x	2x
Asymmetric			down (▼▼)		up (▲▲)		
0	4	$\sqrt{2}$	-1.41				2.83
1	5	$\sqrt{2}$	-1.41		0.71		2.83
2	7	$\sqrt{2}$	-1.41		0.71		
3	11	$\sqrt{2}$			0.71		
Symmetric			down (▼)			up (▲)	
0	4	$\frac{\sqrt{2}}{4}$	-0.35				0.71
1	5	$\frac{\sqrt{2}}{5}$		-0.57		0.28	

Table C2: Far Focus Points of Triangles

i	*t*	Basic	1x	2x	0.5x	1x	2x
Asymmetric			down (▼▼)		up (▲▲)		
0	4	$\frac{\sqrt{2}}{7}$	-0.20				0.40
1	5	$\frac{\sqrt{2}}{4}$	-0.35		0.18		0.71
2	7	$2\frac{\sqrt{2}}{5}$	-0.57		0.28		
3	11	$4\frac{\sqrt{2}}{7}$			0.40		
Symmetric			down (▼)			up (▲)	
0	4	$\frac{\sqrt{2}}{4}$	-0.35				0.71
1	5	$\frac{\sqrt{2}}{5}$		-0.57		0.28	

Table C3: Mid Focus Points of Triangles

i	*t*	Basic	1x	2x	0.5x	1x	2x
Asymmetric			down (▼▼)		up (▲▲)		
0	4	$\frac{\sqrt{2}}{8}$	0.18				-0.35
1	5	$\frac{\sqrt{2}}{5}$	0.28		-0.14		-0.57
2	7	$2\frac{\sqrt{2}}{7}$	0.40		-0.20		
3	11	$4\frac{\sqrt{2}}{11}$			-0.26		
Symmetric			down (▼)			up (▲)	
0	4	$\frac{\sqrt{2}}{8}$	0.18				-0.35
1	5	$\frac{\sqrt{2}}{10}$		0.28		-0.14	

Table C4: Near Focus Points of Triangles

Appendix D: Distance of Triangles from the Origin

The distance from the origin to the nearest side of symmetric triangles:

$$d = \frac{h}{3} = \frac{a\frac{\sqrt{3}}{2}}{3} = a\frac{\sqrt{3}}{6} = s\frac{\sqrt{6}}{t}\frac{\sqrt{3}}{6} = \frac{s}{t}\frac{\sqrt{2}}{2} \qquad (D1)$$

The distance from the origin for asymmetric triangles (basic 2):

$$d_\gamma = a\frac{\sqrt{3}}{6} = s\frac{t-3}{\sqrt{t^2+3}}\frac{\sqrt{3}}{6}\sqrt{6} = s\frac{t-3}{\sqrt{t^2+3}}\frac{\sqrt{2}}{2} = s\frac{2^{i-2}}{\sqrt{2^{2i-2}+3*2^{i-1}+3}}\sqrt{2} \qquad (D2)$$

$$\lim_{i\to\infty} d_\gamma = \lim_{i\to\infty} s\frac{2^{i-2}}{\sqrt{2^{2i-2}+3*2^{i-1}+3}}\sqrt{2} = s\frac{2^{i-2}\sqrt{2}}{2^{i-1}} = s\frac{\sqrt{2}}{2} \qquad (D3)$$

where s =1/2, 1, 2.

i	t	Basic 2	1x s=1	2x s=2	0.5x s=1/2	1x s=1	2x s=2
Asymmetric			down (▼▼)		up (▲▲)		
0	4	$\frac{1}{2}\sqrt{\frac{2}{19}}$	0.16				0.32
1	5	$\frac{1}{2}\sqrt{\frac{2}{7}}$	0.27		0.13		0.53
2	7	$\sqrt{\frac{2}{13}}$	0.39		0.20		
3	11	$2\sqrt{\frac{2}{31}}$			0.25		
∞		$\frac{\sqrt{2}}{2}$			**0.35**		
Symmetric			down (▼)			up (▲)	
0	4	$\frac{\sqrt{2}}{8}$	0.18				**0.35**
1	5	$\frac{\sqrt{2}}{10}$		0.28		0.14	

Table D1: Distance from the Origin to the Nearest Side of Triangles

Copyright: *©2026 Vladimir Saveljev. This is an open-access article distributed under the terms of the Creative Commons Attribution License, which permits unrestricted use, distribution, and reproduction in any medium, provided the original author and source are credited.*